Available online at www.sciencedirect.com

ScienceDirect

Advances in Space Research 54 (2014) 2194–2199

ADVANCES IN SPACE RESEARCH (a COSPAR publication)

www.elsevier.com/locate/asr

Study of the 2013 Lushan M7.0 earthquake coseismic ionospheric disturbances

Peng Chen [a,b,*], Yibin Yao [c,d], Jiajun Chen [c], Wanqiang Yao [a], Xuejun Zhu [a]

[a] College of Geomatics, Xi'an University of Science and Technology, Xi'an 710054, China
[b] State Key Laboratory of Geodesy and Earth's Dynamics, Wuhan 430077, China
[c] School of Geodesy and Geomatics, Wuhan University, Wuhan 430079, China
[d] Key Laboratory of Geospace Environment and Geodesy, Ministry of Education, Wuhan University, Wuhan 430079, China

Received 1 May 2014; received in revised form 9 August 2014; accepted 13 August 2014
Available online 21 August 2014

Abstract

On April 20, 2013, an earthquake of M7.0 occurred in Lushan, Sichuan province, China. This paper investigates the coseismic ionospheric anomalies using GPS (Global Positioning System) data from 23 reference stations in Sichuan province that are a part of the Crustal Movement Observation Network of China (CMONOC). The recorded results show that a clear ionospheric anomaly occurred within 15 min after the earthquake near the epicenter, and the occurrence time of the anomalies recorded by various stations is related to the distance from the epicenter. The maximum anomaly is 0.25 TECu, with a 2 min duration and the distance of the recording station to the epicenter is 83 km. Acoustic waves generated by the crustal vertical movement during the earthquake propagate up to the height of the ionosphere lead to the ionospheric anomaly, and the propagation speed of the acoustic wave is calculated as 0.72 ± 0.04 km/s based on the propagation time and propagation distance, consistent with the average speed of sound waves within a 0–450 km atmospheric height.

Keywords: GPS; Total electron content; Coseismic ionospheric anomalies; Atmospheric acoustic

1. Introduction

Seismic events are one of the most serious natural hazards humanity faces, so the study of the mechanisms of earthquakes and seismic anomalies before and after an event has great significance. Ionospheric anomalies caused by the earthquake have been widespread concerned, and many researchers have studied pre-earthquake ionospheric anomalies. The relationships between an earthquake and pre-earthquake ionospheric anomalies have been studied and researchers have obtained regular behaviors of pre-earthquake ionospheric anomalies (Le et al., 2011, 2013; Liu et al., 2000, 2001, 2006, 2009; Pulinets and Boyarchuk, 2004; Yao et al., 2012a,b; Zhao et al., 2008). In addition, during an earthquake, the atmospheric waves generated by the vertical movement of the ground or sea surface propagate upward and reach the ionosphere inducing the ionospheric electron density anomaly phenomenon known as coseismic ionospheric disturbances (CIDs) (Calais and Minster, 1995; Heki and Ping, 2005; Rolland et al., 2011; Kamogawa and Kakinami, 2013). Various scholars have studied this phenomenon (Calais et al., 1998; Afraimovich et al., 2001; Heki and Ping, 2005; Astafyeva and Heki, 2011; Tsugawa et al., 2011; Saito et al., 2011). Previous technology limitations made it difficult to study the details within CIDs; later, with the emergence of GPS technology, researching CIDs using the ionospheric TEC (total electron content) obtained by

* Corresponding author at: College of Geomatics, Xi'an University of Science and Technology, Xi'an 710054, China.
E-mail address: chenpeng0123@gmail.com (P. Chen).

http://dx.doi.org/10.1016/j.asr.2014.08.014
0273-1177/

GPS technology became a research focus. Astafyeva et al. (2009) studied the 1994 Kurile M8.1 earthquake coseismic ionospheric disturbances and found that there is a correlation between the time of appearance of a CID and its distance to the epicenter, and that CIDs have two different velocity components, the Rayleigh surface wave velocity (3–4 km/s) and sound velocity (0.6–1.0 km/s), respectively. Choosakul et al. (2009) showed that the 4-min periodic TEC variations occurred 1 h after the Sumatra-Andaman earthquake in 2004 and continued for longer than 4 h. Liu et al. (2010) found that the 1999 Taiwan Chi-Chi earthquake also caused significant CIDs. Heki (2011) detected clear precursory positive anomaly of ionospheric TEC around the focal region. It started ~40 minutes before the earthquake and reached nearly ten percent of the background TEC. Astafyeva et al. (2013) showed that the amplitude of coseismic total electron content variations is larger after more powerful earthquakes, and stronger earthquakes were characterized by a longer negative phase in coseismic perturbations. Cahyadi and Heki (2013) studied the 2007 Bengkulu Mw8.5 earthquake and the 2005 Nias Mw8.6 earthquake coseismic ionospheric disturbances, and results indicated that 10–16 min after the earthquakes, significant ionospheric disturbances occurred north of the epicenters, and the velocity of the sound waves generated by the seismic events was ~0.7 km/s.

In this paper, using GPS data from the Crustal Movement Observation Network of China (CMONOC) reference stations in Sichuan, we investigate the coseismic ionospheric disturbances after the April 20, 2013 Lushan M7.0 earthquake and derive the characteristics of the CIDs caused by this event.

2. Data and data processing method

The Lushan M7.0 earthquake occurred on April 20, 2013 at 00:02:46 UT, from a depth of 14 km, with the epicenter occurring at 30.28°N, 102.95°E, located in the southern section of the Longmen tectonic belt, and was a thrust earthquake.

We use raw GPS data supplied by CMONOC with data sampling rate of 30 s. CMONOC is a high-precision, high spatial and temporal resolution observation network, mainly providing GNSS observations combined with a variety of other techniques, and consists of 260 continuous observation stations and 2000 occasional observation stations primarily used to monitor crustal movement, gravity field, tropospheric water vapor content, and ionospheric ion concentration related to the Chinese mainland.

GPS satellites transmit dual-frequency signals of 1575.42 and 1227.60 MHz, corresponding to wavelengths of 19.03 and 24.42 cm, respectively. Since the ionosphere is a dispersive medium, GPS signals suffer an ionospheric delay dependent on the signal frequency; therefore, using dual-frequency phase observations can provide the total electron content $STEC_\varphi$ along the GPS signal propagation path. During CIDs detection and analysis only the relative change of the STEC, $STEC_\varphi$, is determined with high accuracy and has been considered a suitable method for the detection of CIDs. The formula of the $STEC_\varphi$ calculation using GPS dual frequency phase observations can be written as (Calais and Minster, 1995):

$$STEC_\varphi = \frac{f_1^2 f_2^2}{40.3 \cdot (f_1^2 - f_2^2)} \cdot [(\lambda_1 \varphi_1 - \lambda_2 \varphi_2) + N + \varepsilon_\varphi] \quad (1)$$

where f_1 and f_2 are the GPS carrier frequencies; φ_1 and φ_2 are dual-frequency carrier phase measurements of the two frequencies (in units of cycle); λ_1 and λ_2 are the GPS carrier wavelengths; N is the ambiguity of phase measurements; ε_φ is the observation noise. Currently, the carrier phase measurement accuracy of a geodesy type GPS receiver is 0.2–0.3 mm, and if we ignore the impact of ambiguity, then the accuracy of $STEC_\varphi$ is 0.0027–0.0040 TECu, well suited for detecting small ionospheric disturbances.

GPS satellites have relatively smooth orbits, so if a station continuously tracks the same satellite, the obtained STEC should also be relatively smooth under quiet ionosphere conditions, but fluctuations in the TEC occur a short time after an earthquake (the CIDs caused by the earthquake). However, the change rate of the STEC is large and it is difficult to detect any slight anomalies directly through STEC. For this reason, Liu et al. (2004) proposed an ionospheric anomaly detection method through a single difference operation of the TEC, $dTEC$, but there are still large fluctuations that mask small anomalies using this method. We propose differencing the TEC again to obtain d^2TEC, where the change of d^2TEC is more stable and allows easier detection of miniscule fluctuations in the ionosphere. $dTEC$, and d^2TEC are calculated by Eq. (2):

$$\begin{aligned} dTEC_i &= TEC_{i+1} - TEC_i \\ dTEC_{i+1} &= TEC_{i+2} - TEC_{i+1} \\ d^2TEC_i &= dTEC_{i+1} - dTEC_i \end{aligned} \quad (2)$$

Using a single layer ionosphere assumption in data processing, namely that all electrons in the ionosphere are concentrated in an infinitely-thin layer at a certain height (450 km in this article). The intersection point of the receiver and satellite connection path and the thin layer is named the Ionospheric Pierce Point, IPP, and the projection point of the IPP on the ground is named the Sub Ionospheric Point, SIP.

The IPP coordinate when a CID occurs based on the CID's time of occurrence and the distance between the epicenter and the IPP is used to calculate the propagation velocity of atmospheric seismic waves generated by an earthquake.

Fig. 1 shows the epicenter of the Lushan earthquake and the distribution map of the 23 CMONOC GPS continuous tracking stations in Sichuan province discussed in this paper, where the blue star denotes the location of the epicenter. As can be seen from the figure, the GPS continuous tracking stations are very close to the epicenter, where the

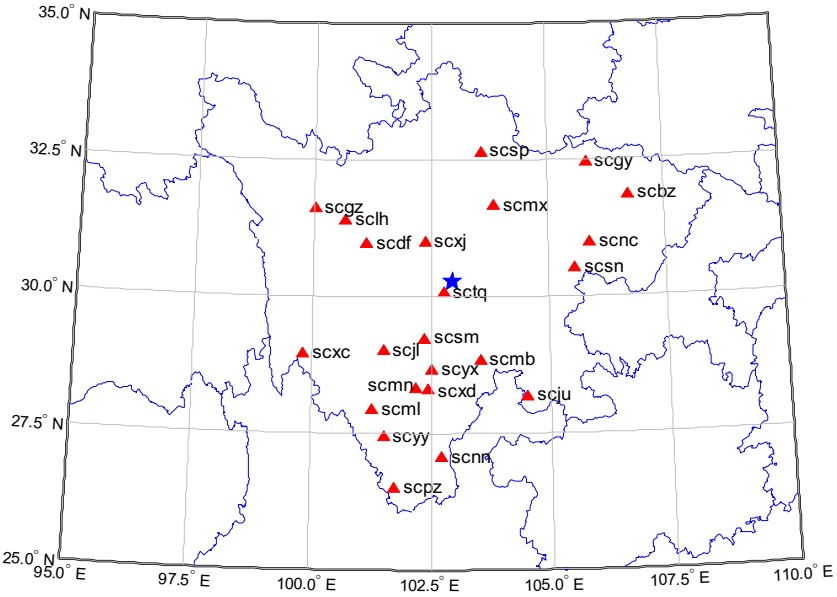

Fig. 1. Location map of the April 20, 2013 earthquake epicenter and existing CMONOC GPS continuous tracking stations in Sichuan province.

nearest station, SCTQ, is only 55 km from the epicenter, and the furthest station, SCPZ, is only 467 km from the epicenter. The high distribution density of the tracking stations can effectively capture any weak ionospheric anomalies.

2.1. Analysis

Satellites and receivers formed a dense IPP distribution around the epicenter, but only a small number of IPPs in this region were useful when the CID reached the height of the ionosphere, so only a small number of satellites were able to monitor the CID. Fig. 2 shows the STEC time series diagram using dual-frequency phase observations from nine PRN15 satellite tracking stations near the epicenter during 00:00–01:00 UT, April 20. The figure shows that the STEC is smoother in the quiet period, but produces short-term fluctuations as the waves of seismic origin spread to the height of the ionosphere, and later return to normal. STEC obtained by stations SCYX, SCYY, SCXD, SCMN, SCML, and SCJL indicate ionospheric anomalies, which occurred within 10–13 min after the earthquake, and SCYX, SCXD and SCMN recorded the most significant anomalies. The distances from the abnormal occurrence locations to the epicenter were 43.7, 59.9, and 46.2 km, and the amplitudes of the anomalies were 0.09, 0.08, and 0.09 TECu, all with durations of 90 s.

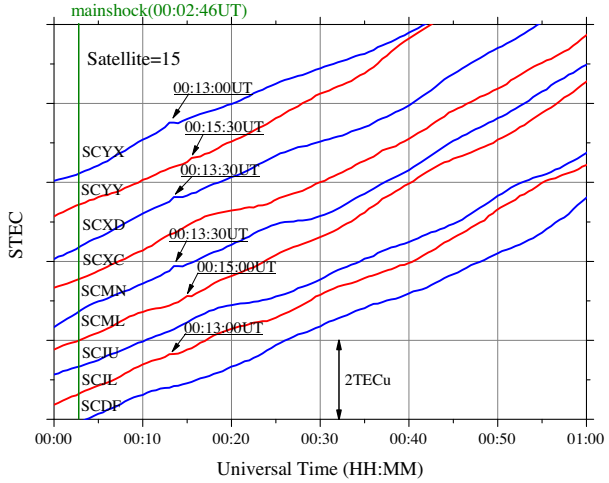

Fig. 2. Nine stations obtained PRN15 satellite STEC time series curves at 00:00–01:00 UT, April 20. In the figure, the green line represents the moment of the earthquake, and the time stamps represent the moment obvious disturbances were detected by the tracking stations. (For interpretation of the references to color in this figure legend, the reader is referred to the web version of this article.)

Fig. 3(a) and (b) show the time series curves calculated by $dTEC$ and d^2TEC during 00:00–01:00 UT on April 20, 2013, respectively. The figure indicates that single difference can eliminate the trend term of STEC, and $dTEC$ varies within ±0.1 TECu, but there are still obvious fluctuations. Differencing $dTEC$ again to obtain d^2TEC, more stable curves are obtained, and fluctuations are very close to zero under quiet conditions, but obvious fluctuations appear when the CID occurs. The double differencing method we propose is very suitable for the detection of coseismic ionospheric disturbances.

Fig. 4 shows the STEC and d^2TEC time series of the SCJU tracking station and PRN21 observation station. Fig. 5(a) shows that very significant ionosphere disturbance occurred within 10 min after the earthquake, first appearing as positive anomalies with a maximum amplitude of 0.1 TECu, and then became negative anomalies that lasted approximately two min before the STEC returned to normal. It can be seen from Fig. 5(b) that the d^2TEC curve is close to zero and relatively stable in ionospheric quiet

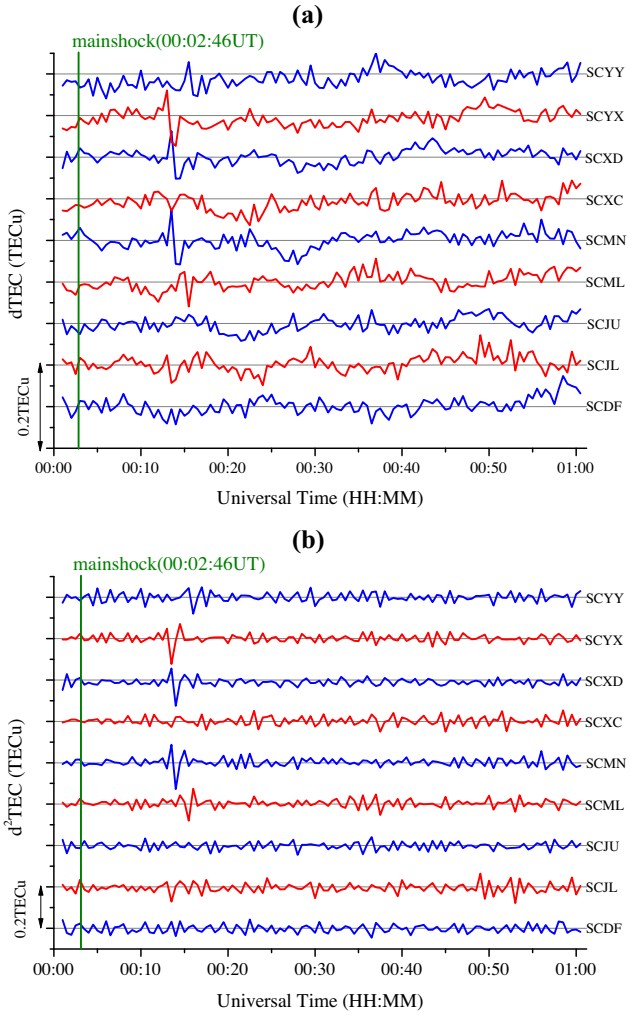

Fig. 3. *dTEC* and d^2TEC PRN15 time series curves of 9 GPS tracking stations during 00:00–01:00 UT, April 20, 2013.

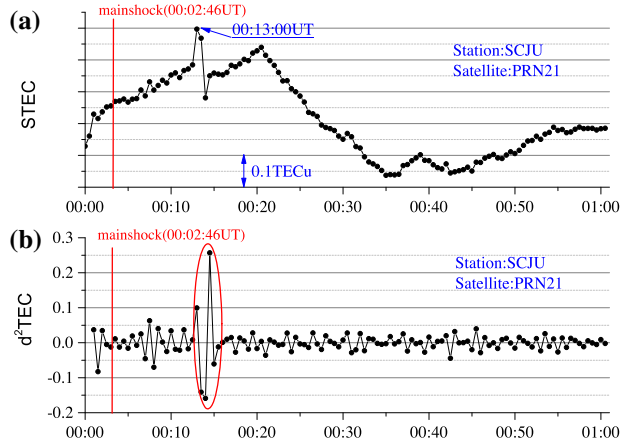

Fig. 4. The STEC and d^2TEC time series curves obtained from SCJU and PRN21 data collected from 00:00–01:00 UT on April 20, 2013.

conditions, with fluctuations within ±0.05 TECu, and the curve jumps sharply when the ionosphere disturbance induced by the earthquake occurs (shown in the red ellipse), with a maximum amplitude of over 0.25 TECu.

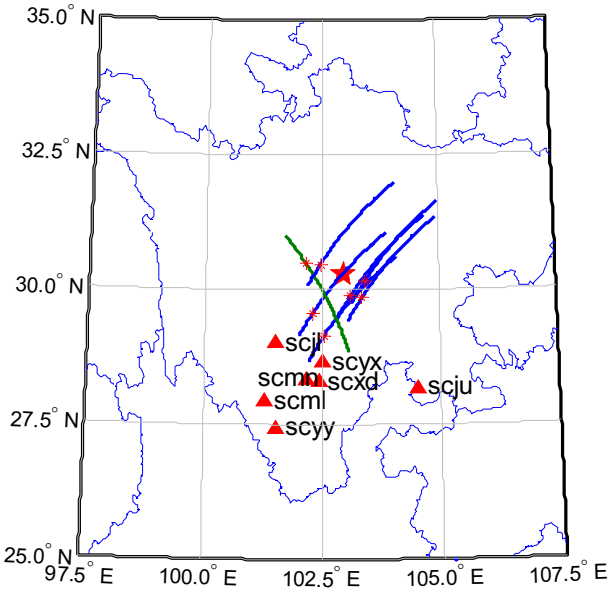

Fig. 5. Map of the CID detection stations and satellites.

Table 1 shows the CIDs occurrence time, the geodetic coordinates of the IPPs and the calculated atmospheric acoustic propagation velocity calculated from 7 tracking stations that detected the CIDs. From the table, the calculated velocity of wave propagation by the different stations varied within 0.63–0.77 km/s with an average of 0.72 km/s, and the standard deviation was 0.06 km/s. This result is very close to the 0.69 ± 0.04 km/s calculated by Cahyadi and Heki (2013) for the 2007 Bengkulu earthquake.

Fig. 5 shows the location map of the ionospheric anomaly, where the star denotes the epicenter, the triangle denote the tracking stations that detected the CIDs, the blue curves are the SIP trajectory of a PRN15 satellite, and SCJL, SCMN, SCYX, SCXD, SCML, and SCYY are the 6 tracking stations during 00:00–01:00 UT, the green curve denotes the PRN21 satellite and SCJU, and the asterisk indicates the SIP location when the coseismic ionospheric disturbances occurred. It can be seen that due to the relatively small magnitude of the earthquake, the ionospheric disturbances caused by the earthquake were limited to a small area near the epicenter, and the maximum distance of the CIDs from the epicenter was only 133.6 km, while there were no obvious ionospheric disturbances at further distances.

Fig. 6 shows the relationships among d^2TEC, CIDs occurrence time, and the distance to the epicenter. The figure shows that under quiet conditions the d^2TEC is very close to zero, but shows a disturbance with amplitude of −0.15–0.25 TECu when the CIDs occur. The detection occurrence time of the CIDs varies with the distance to the epicenter, and the best connection line shown as the solid red line represents the average speed of the seismic wave during propagation from the epicenter to the IPPs and is almost the same as the 0.72 ± 0.06 km/s calculated in Table 1.

Table 1
Occurrence moment of the CIDs, geodetic coordinates of IPPs, and wave propagation velocity from 7 tracking stations that detected the April 20, 2013 CIDs.

Station	Occurrence time (UT)	Latitude (degree)	Longitude (degree)	Propagation velocity (km/s)
SCJL	0:13:00	30.4800	102.4500	0.76
SCJU	0:13:00	30.5027	102.1339	0.77
SCML	0:15:00	29.5700	102.2900	0.65
SCMN	0:13:30	29.8799	103.0881	0.72
SCXD	0:13:30	29.8477	103.3309	0.73
SCYX	0:13:00	30.1476	103.3887	0.76
SCYY	0:15:30	29.1395	102.5238	0.63

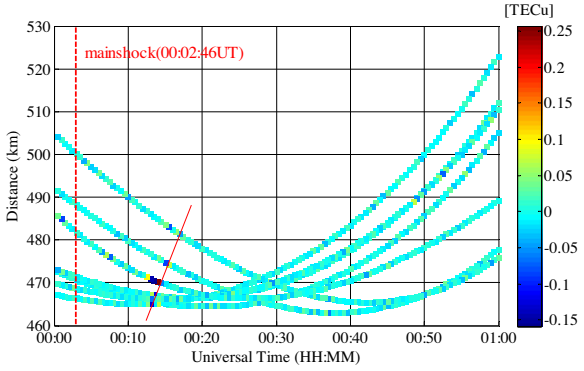

Fig. 6. Relationships among d^2TEC, the occurrence moment of the CIDs and the distance from the epicenter. UT time is the abscissa, the distance between an IPP and the epicenter is the vertical coordinate, d^2TEC is described with different colors (the colored bar), the red dotted line indicates the earthquake moment, and the thin red solid line indicates the connection line of the maximum values of d^2TEC. (For interpretation of the references to color in this figure legend, the reader is referred to the web version of this article.)

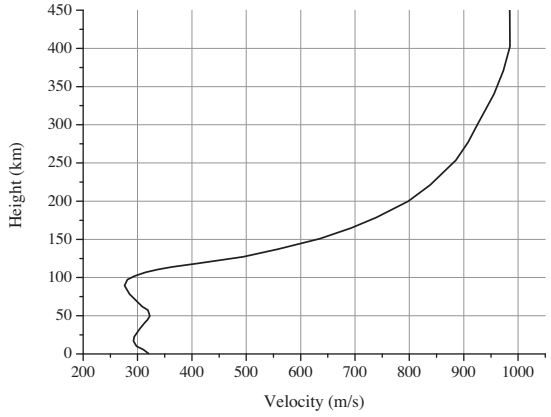

Fig. 7. Wave transmission velocity diagram within 0–450 km from the ground (Calais et al., 1998).

Fig. 7 shows the relationship between the propagation velocity of the acoustic wave and its height from the ground within 0–450 km. The propagation velocity of the acoustic wave is about 980 m/s at the ionosphere height, much larger than the propagation velocity of 320 m/s at ground level. The propagation velocity of sound has small variation under a 100 km height; the velocity decreases with increasing height within 0–20 and 50–85 km height ranges, and within 20–50 km the velocity increases with increasing height. The propagation velocity increases rapidly with increasing height from 100 to 400 km and essentially remains constant from 400 to 450 km. According to the figure, at different heights from the ground to the ionospheric height, the average acoustic wave propagation velocity is 710.03 m/s, and is very close to the Lushan earthquake wave average propagation velocity of 0.72 km/s calculated in this paper, indicating that CIDs are indeed caused by sound waves generated by earthquakes that propagate to the ionosphere height, and also indicates that the methods and results applied in this article are valid.

3. Conclusion

We investigate the April 20, 2013 Lushan M7.0 earthquake coseismic ionospheric anomalies. The STEC data obtained by CMONOC GPS observations is analyzed, and the results show that the ionospheric anomalies occurred near the epicenter within 10–13 min after the earthquake. Through the studies of the epicenter's location of CIDs, and the propagation velocity of the seismic waves generated by the earthquake, the following conclusions apply:

(1) The magnitude and duration of CIDs caused by this earthquake are relatively small, and the CIDs locations are very close to the epicenter due to the relatively small magnitude of the earthquake;
(2) The results show that seismic waves propagate from the ground to the height of the ionosphere with an average velocity of 0.72 ± 0.06 km/s, a very close result to the average velocity of sound wave propagation (710 m/s) within a 0–450 km atmospheric height, indicating that CIDs are indeed caused by sound waves that are generated by earthquakes and propagate up to the ionosphere.

However, we present a preliminary study of the CIDs after the Lushan earthquake, and examine only the component caused by the spread of acoustic velocity waves. Further studies to determine whether higher speed transmission components exist during a seismic event should be carried out.

Acknowledgments

Thanks to CMONOC to provide the GPS data. The project supported by State Key Laboratory of Geodesy and Earth's Dynamics Fund (SKLGED2013-4-10-EB), State Key Laboratory of Information Engineering in Surveying Mapping and Remote Sensing Fund (13S03), Key Laboratory of Geo-informatics of State Bureau of Surveying and Mapping Fund (201318), the Surveying and Mapping Foundation Research Fund Program, State Bureau of Surveying and Mapping (12-01-07) and Xi'an University of Science and Technology Cultivation Fund (201204).

References

Afraimovich, E.L., Perevalova, N.P., Plotnikov, A.V., et al., 2001. The shock-acoustic waves generated by earthquakes. Ann. Geophys. 19, 395–409.

Astafyeva, E., Heki, K., 2011. Vertical TEC over seismically active region during low solar activity. J. Atmos. Solar Terr. Phys. 73 (13), 1643–1652.

Astafyeva, E., Heki, K., Kiryushkin, V., et al., 2009. Two-mode long-distance propagation of coseimic ionosphere disturbances. J. Geophys. Res. 114, A10307.

Astafyeva, E., Shalimov, S., Olshanshaya, E., et al., 2013. Ionospheric response to earthquakes of different magnitudes: larger quakes perturb the ionosphere stronger and longer. Geophys. Res. Lett. 40, 1–7.

Cahyadi, M.N., Heki, K., 2013. Ionospheric disturbances of the 2007 Bengkulu and the 2005 Nias earthquakes, Sumatra, observed with a regional GPS network. J. Geophys. Res. 118, 1675–1681.

Calais, E., Minster, J.B., 1995. GPS detection of ionospheric perturbations following the January 17, 1994, Northridge earthquake. Geophys. Res. Lett. 22 (9), 1045–1048.

Calais, E., Bernard Minster, J., Hofton, M., 1998. Ionospheric signature of surface mine blasts from global positioning system measurements. Geophys. J. Int. 132 (1), 191–202.

Choosakul, N., Saito, A., Iyemori, T., et al., 2009. Excitation of 4-min periodic ionospheric variations following the great Sumatra–Andaman earthquake in 2004. J. Geophys. Res. 114, A10313.

Heki, K., 2011. Ionospheric electron enhancement preceding the 2011 Tohoku-Oki earthquake. Geophys. Res. Lett. 38, L17312.

Heki, K., Ping, J., 2005. Directivity and apparent velocity of the coseismic ionospheric disturbances observed with a dense GPS array. Earth Planet. Sci. Lett. 236 (3), 845–855.

Kamogawa, M., Kakinami, Y., 2013. Is an ionospheric electron enhancement preceding the 2011 Tohoku-Oki earthquake a precursor? J. Geophys. Res. Space Phys. 118, 1751–1754.

Le, H., Liu, J.Y., Liu, L., 2011. A statistical analysis of ionospheric anomalies before 736 M6.0+ earthquakes during 2002–2010. J. Geophys. Res. 116, A02303. http://dx.doi.org/10.1029/2010JA015781.

Le, H., Liu, L., Liu, J.Y., et al., 2013. The ionospheric anomalies prior to the M9.0 Tohoku-Oki earthquake. J. Asian Earth Sci. 62, 476–484.

Liu, J.Y., Chen, Y.I., Pulinets, S.A., et al., 2000. Seimo-ionospheric signatures prior to $M \geqslant 6.0$ Taiwan earthquakes. Geophys. Res. Lett. 27 (19), 3113–3116.

Liu, J.Y., Chen, Y.I., Chuo, Y.J., et al., 2001. Variations of ionospheric total electron content during the Chi-Chi earthquake. Geophys. Res. Lett. 28 (7), 1383–1386.

Liu, J.Y., Lin, C.H., Tsai, H.F., et al., 2004. Ionospheric solar flare effects monitored by the ground-based GPS receivers: theory and observation. J. Geophys. Res. 109, A01307.

Liu, J.Y., Chen, Y.I., Chuo, Y.J., et al., 2006. A statistical investigation of preearthquake ionospheric anomaly. J. Geophys. Res. 111, A05304.

Liu, J.Y., Chen, Y.I., Chen, C.H., et al., 2009. Seismoionospheric GPS total electron content anomalies observed before the 12 May 2008 Mw7.9 Wenchuan earthquake. J. Geophys. Res. 114, A04320.

Liu, J.Y., Tsai, H.F., Lin, C.H., et al., 2010. Coseismic ionospheric disturbances triggered by the Chi-Chi earthquake. J. Geophys. Res. 115, A08303.

Pulinets, S.A., Boyarchuk, K.A., 2004. Ionospheric Precursors of Earthquakes. Springer, New York, Berlin.

Rolland, L.M., Lognonné, P., Astafyeva, E., et al., 2011. The resonant response of the ionosphere imaged after the 2011 off the Pacific coast of Tohoku Earthquake. Earth Planets Space 63 (7), 853–857.

Saito, A., Tsugawa, T., Otsuka, Y., et al., 2011. Acoustic resonance and plasma depletion detected by GPS total electron content observation after the 2011 off the Pacific coast of Tohoku Earthquake. Earth Planets Space 63 (7), 863–867.

Tsugawa, T., Saito, A., Otsuka, Y., et al., 2011. Ionospheric disturbances detected by GPS total electron content observation after the 2011 off the Pacific coast of Tohoku Earthquake. Earth Planets Space 63 (7), 875–879.

Yao, Y.B., Chen, P., Zhang, S., et al., 2012a. Analysis of pre-earthquake ionospheric anomalies before the global $M = 7.0+$ earthquakes in 2010. Nat. Hazards Earth Syst. Sci. 12 (3), 575–585.

Yao, Y.B., Chen, P., Wu, H., et al., 2012b. Analysis of ionospheric anomalies before the 2011 Mw9.0 Japan earthquake. Chin. Sci. Bull. 57 (5), 355–365.

Zhao, B., Wang, M., Yu, T., et al., 2008. Is an unusual large enhancement of ionospheric electron density linked with the 2008 great Wenchuan earthquake? J. Geophys. Res. 113, A11304.